Supporting Information

# In-situ dopant-induced nano-crystallization of rare-earth-fluoride crystals in phase-separated networks for highly-efficient photoemission and photonic devices

Zaijin Fang, Jianfeng Li, Li-Peng Sun, Yanyan Zhi, Yi Long, Shupei Zheng, Zhi Chen*, Jianrong Qiu, and Bai-ou Guan*

## Experimental Section

**Materials.** The oxyfluoride glass with composition of $SiO_2/K_2O/Al_2O_3/YbF_3/KF$= 54/10/15/6/15 (in mol%) was melted at 1550 $^oC$ for 60 min to fabricate precursor glass (PG). Then the PGs were heat treated at 700 $^oC$ for 2h to obtain nano-crystallized glass ceramics (NGCs) containing $KYb_2F_7$ nanocrystals. The PG with composition of $SiO_2/Na_2O/Al_2O_3$/ NaF/YF=55/16/10/12/7 (in mol%) was fabricated at 1450 $^oC$ for 30 min. Then the PGs were heat treated at 650 $^oC$ for 2h to obtain NGCs containing β-$NaYF_4$ nanocrystals.

In order to fabricate the microspheres, glass fibers were firstly drawn from the melt of 70Si-PG by using a diamond tip.[1] The glass fibers were prepared by quickly drawing at an appropriate glass melt viscosity, which was initially cleaned ultrasonically and then using a number of hydrofluoric acid washes. Then a taper from the glass fiber was first prepared by vertically suspending it on a 3D adjustable mount. A small region of the fiber was heated by a $CO_2$ laser beam focused to about 150 μm, and we increased the power of the laser until the glass fiber rapidly elongated into a taper. We were able to control the waist diameter of the taper by adjusting the distance between the glass fiber and the laser beam; a taper diameter of about 3 μm was selected, and it was then cut into a half-taper by shining the laser at the center of the waist region. Next, we heated the tip of the half-taper by the $CO_2$ laser beam until it was near the melting temperature of the glass. The surface tension of the glass creates a microsphere from the tip. During the heating process, the tapered fiber was moved slowly

along the half-taper in order to enlarge the size of the glass microsphere. Using the described method, we prepared the $Er^{3+}$ doped 70Si-PG microspheres with diameters ranging from 30 to 100 μm. Finally, the PG microspheres were covered by a quartz evaporating dish and put into the furnace for the heat treatements at 520 $^{o}$C for 5 and 10 h to obtain NGC microspheres, which were used as gain matrices as well as resonant cavities to realize more efficient lasers.

**Simulation.** MD simulations were applied to simulate the glass networks via LAMMPS (Large-scale Atomic/Molecular Massively Parallel Simulator).[2] The pairwise interatomic potentials with Buckingham form were used. This potential is based on a rigid ionic model with partial charges to handle the partial covalency of glass and is given by the combination of two parts: the long-range Coulombic potential and the short-range forces. The exact expression (1) of the model potential is :

$$U(r) = \frac{z_i z_j e}{r} + A_{ij} e^{-r/\rho_{ij}} - \frac{C_{ij}}{r^6} \quad (1)$$

Where $z_i$, $z_j$, refer to the charge of ions, and $A_{ij}$, $r_{ij}$, $C_{ij}$ are parameters which have been proved to be well fitted to its original structure. Due to the unphysical fusion deficiency of Buckingham form potential, the potential is refined at short atomic distance by adding a repulsive term of the expression (2):

$$U(r)=B/ r^{n}+D*k^{2} \quad (2)$$

Verlet Leap-Frog algorithm with a time step of 1 fs and pppm summation with a cutoff distance of 10 Å was employed to integrate the equation of motion and caculate Coulombic interactions, respectively. The short-range interaction cutoff was also set to 10 Å. Berendsen thermostat and barostat was employed to control temperature and pressure during simulation.

Glass structure was obtained through a melt-quench process. Firstly, the initial structure was increased to 6000 K with NVT ensemble and relaxed with NVE ensemble at 2000 K, 4000 K for 50000 steps, 6000 K for 100000 steps. Then, the structure cool to 300 K at a nominal speed of 4 K/ps and relaxed for 50000 steps with NVE ensemble before collecting

final structure. Finally, MD trajectories of the final structure at 300 K under NVE ensemble were recorded every 100 steps for other analysis.

## Results and discussion

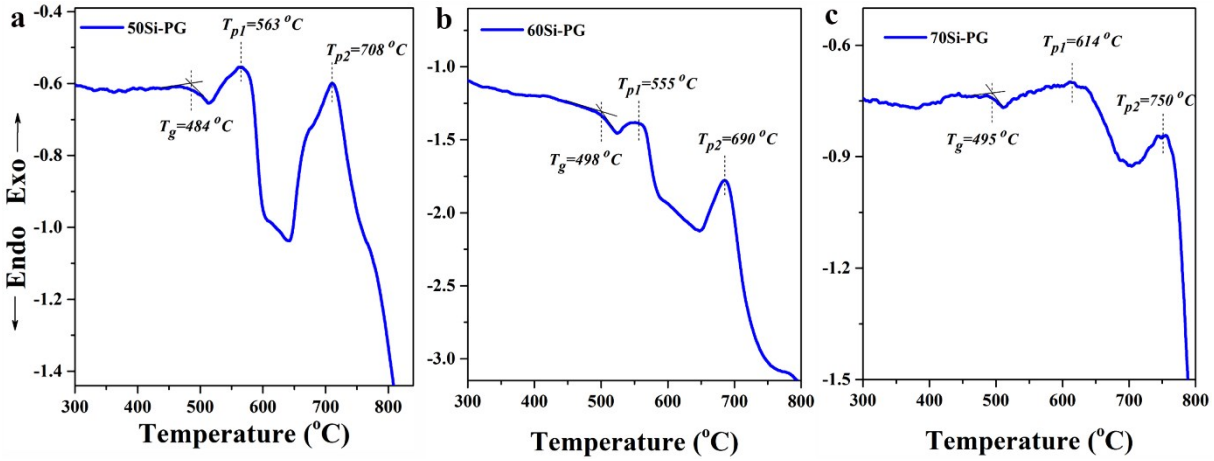


**Figure S1.** DSC curves of (a) 50, (b) 60 and (c) 70Si-PGs. The transition temperature (Tg) of the 50Si, 60Si and 70Si-PG is 484, 498 and 495 °C, respectively. Since fluorides exhibit lower viscosity, the first crystallization peaks in the DSC curves are attributed to the crystllization of fluoride crystals. For the controllable precipitation of fluoride nanocrystals, the heat treatment temperature should be set between the $T_g$ and the first crystallization peak temperature ($T_{p1}$). The heat treatment temperatures of the three PGs were set to 520 °C to obtain NGCs containing fluoride nanocrystals.

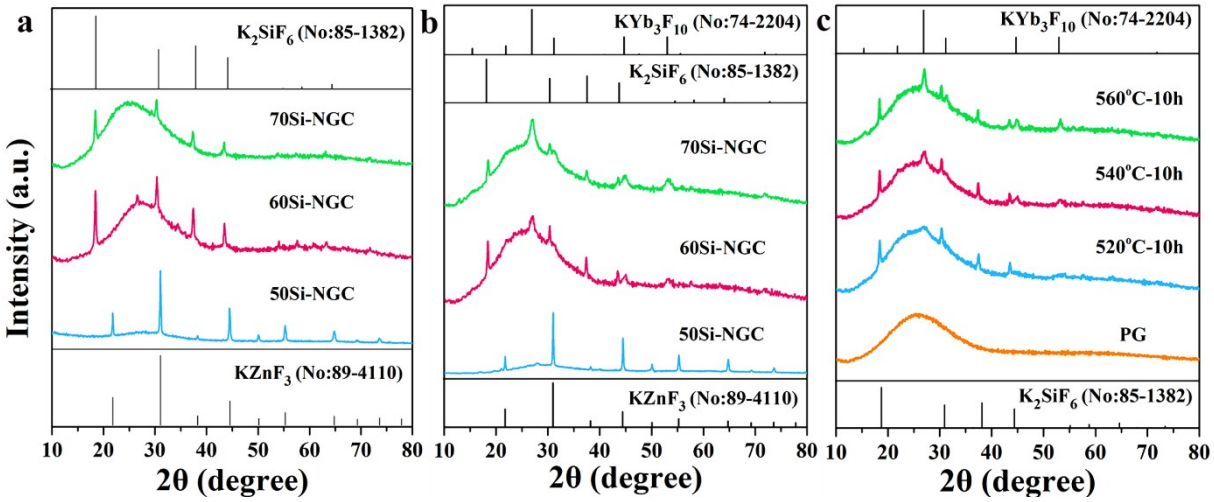


**Figure S2.** (a) XRD patterns of the un-doped NGCs. $KZnF_3$ (89-4110) crystals are precipitated in the un-doped 50Si-NGCs, while $K_2SiF_6$ crystals (85-1382) are precipitated in the un-doped 60 and 70Si-NGCs. (b) XRD patterns of the $0.5Yb^{3+}$ doped NGCs. Apart from the crystalline peaks of $K_2SiF_6$ crystals, the diffraction peaks at 26.9, 30.9, 44.8 and 53.2 ° are also observed in the XRD patterns of $0.5Yb^{3+}$ doped 60 and 70Si-NGCs, which are attributed to the diffractions of (202), (004), (224) and (422) crystal facets of the cubic $KYb_3F_{10}$ (74-2204), respectively. However, no obvious peak attributed to $KYb_3F_{10}$ crystals is observed in the XRD pattern of $0.5Yb^{3+}$ doped 50Si-NGC. As calculated by Scherrer formula, the average size of $KZnF_3$ and $KSiF_6$ crystals in 50 and 60Si-GCs is 40.5 and 22.8 nm, respectively, while that of $KYb_3F_{10}$ crystals in 70Si-GC is as small to 8.1 nm. The crystalline volume fraction of $KYb_3F_{10}$ crystals in 70Si-GC is calculated to about 1.2% from the XRD pattern, while that of $KZnF_3$ crystals is as high to 15.3%. (c) XRD patterns of the $0.3Yb^{3+}$ doped 70Si-PG and NGCs. The XRD pattern of PG exhibits broad band due to amorphous state. The diffraction peaks of $KYb_3F_{10}$ crystals are obviously enhanced when the heating temperature increases from 520 to 560 °C.

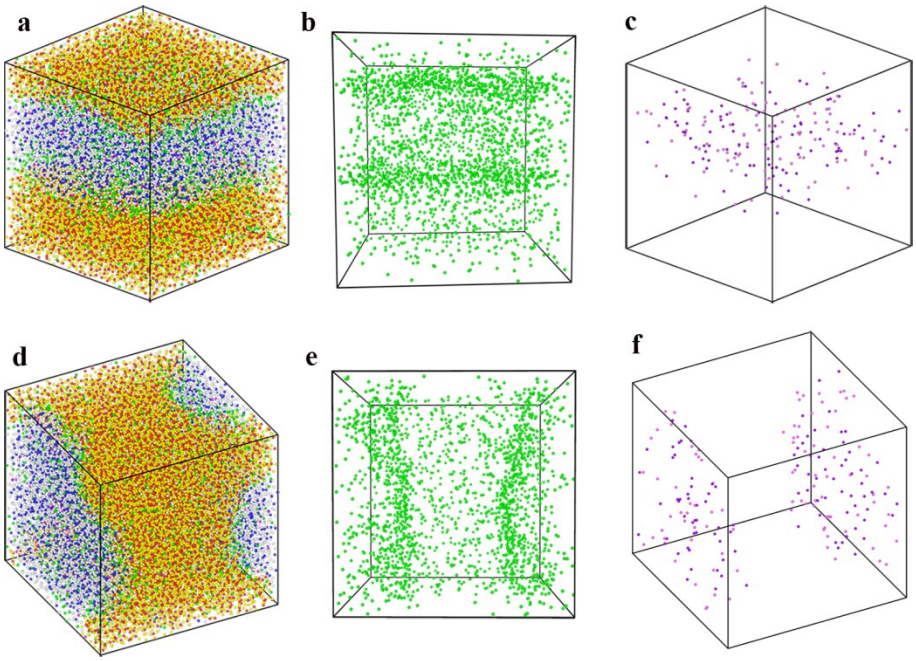


**Figure S3.** MD simulation snapshot of the local networks for 1.5$Yb^{3+}$ doped (a) 50Si and (d) 60-PGs. Distribution patterns of (b) K and (c) Yb elements corresponding to the structure in (a). Distribution patterns of (e) K and (f) Yb elements corresponding to the network in (d). Yellow ball represents Si; red, O; white, F; blue, Zn; green, K; Yb; pink, Yb.

The glass networks of 50Si and 60Si-PGs also exhibit phase-separated structures and the separate fluoride glass nanophases are vividly observed in the three glass structures. Interpenetrating phase-separation is observed in the structure of 50Si-PG (**Figure S3**(a)). For 60Si-PG, droplet phase-separation emerges from the interpenetrating phase-separation region (**Figure S3**(d)). In the networks of the two glasses, K elements prefer distribute in the interface of silicon-rich and fluorine-rich phases to balance the valence of non-bridging oxygens and $F^-$ bond (**Figure S3**(b) and (e)). The residual K elements free in the breaks of networks.

For 50Si-PG, more $ZnF_2$ and KF are introduced into the glass and the local networks exhibit lower viscosity, $KZnF_3$ crystals are precipitated from the fluoride-rich regions by the heat treatments (**Figure S2**(a)). For 60Si-GC, the glass networks exhibit high viscosity due to the decrease of $ZnF_2$ and KF in fluorine-rich regions,

the crystallization barriers for $KZnF_3$ are difficult to overcome by the heat treatments. $K_2SiF_6$ crystals are precipitated near the interfaces of the two phases due to the interface induced effects and the lower viscosity via the gathering of $K^+$ in the un-doped 60Si-NGC (**Figure S2**(b)).

More importantly, the distribution patterns of Yb (**Figure S3**(c) and (f)) in 50Si and 60Si-PG match well with that of the separated fluoride networks, indicating that $Yb^{3+}$ ions are all distributed within the fluoride networks. Comparing to the 70Si-PG, the distribution of Yb in 50Si-PG is more dispersive and the ionic distance of $Yb^{3+}$ is long, which is not beneficial for the precipitation of $KYb_3F_{10}$ crystals in spite of the doping of $Yb^{3+}$ into the glass (**Figure S2**(b)). For the 60Si-PG, the distribution of Yb is more compact than 50Si-PG but more dispersive than 70 Si-PG. Therefore, $KYb_3F_{10}$ crystals can precipitate in 60Si-NGC during heat treatments but the crystalline volume fraction is smaller than that in 70Si-NGC (**Figure S2**(b)).

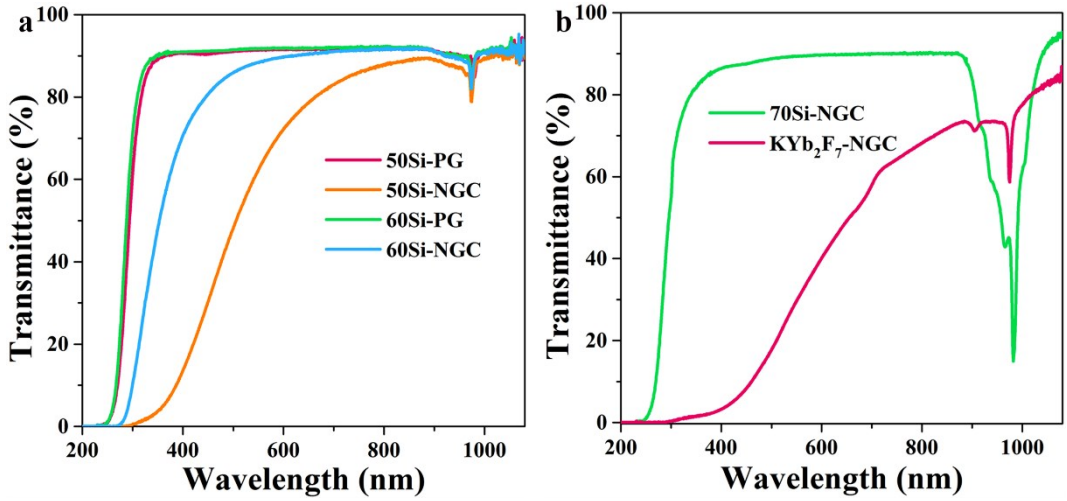


**Figure S4.** (a) Transmission spectra of $0.5Yb^{3+}$ doped 50, 60Si-PGs and NGCs. The transmittance of 50Si-GC dramatically falls down to 40% at 500 nm after the heat treatment. This is caused by the vast precipitation of $KZnF_3$ crystals possessing large size. The transmittance of 60Si-GC is also decreased due to the precipitation of $K_2SiF_6$ and $KYb_3F_{10}$ nanoparticles. (b) Transmission spectra of $KYb_2F_7$ NGC and $1.0Yb^{3+}$ doped β-$NaYF_4$ NGC. The NGC containing β-$NaYF_4$ crystals possesses extremely low transmittance in visible region due to the serious scattering of crystal particles and the $KYb_2F_7$ NGC exhibit huge absorption around 976 nm due to the high concentration of $Yb^{3+}$.

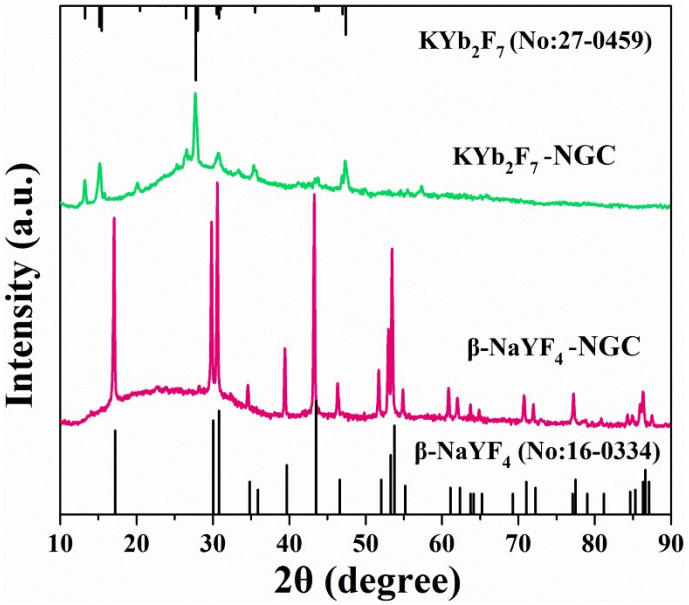


**Figure S5.** XRD patterns of NGCs containing $KYb_2F_7$ and β-$NaYF_4$ crystals. The XRD patterns of the NGCs match well with the JCPDS Cards of $KYb_2F_7$ (No: 27-0459) and β-$NaYF_4$ (No: 16-0334) crystals, respectively. These prove that $KYb_2F_7$ and β-$NaYF_4$ crystals are successfully precipitated in the traditional NGCs, respectively.

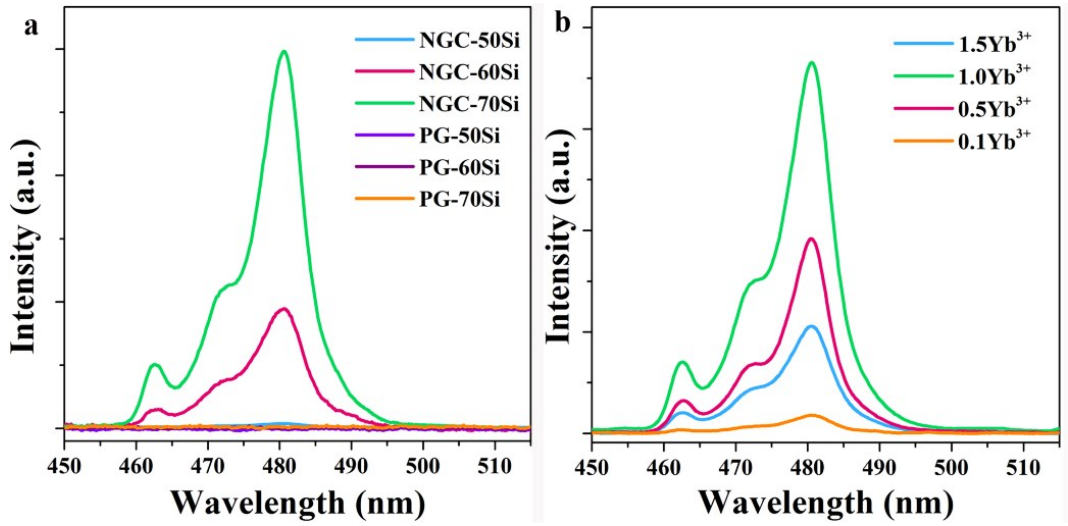


**Figure S6.** (a) UC emission spectra of $0.5Yb^{3+}$ doped PGs and NGCs. No emission peak is observed in the spectra of the PGs. Excited by using a 980 nm laser diode, emission peaks around 480 nm attributed to the UC emission of $Yb^{3+}$-$Yb^{3+}$ pairs are observed in the spectra of 60 and 70Si-NGCs. However, no obvious emission peak is observed in the spectra of 50Si-NGC. (b) UC emission spectra of $Yb^{3+}$ doped 70Si-NGCs heat treated at 520 $^{o}$C for 10 h. The intensity of UC emission of NGC is increased when the doping concentration increases from 0.1 to 1.0 mol%. Then the emission intensity decreases when the doping concentration is further increased to 1.5 mol% due to concentration quenching effect.

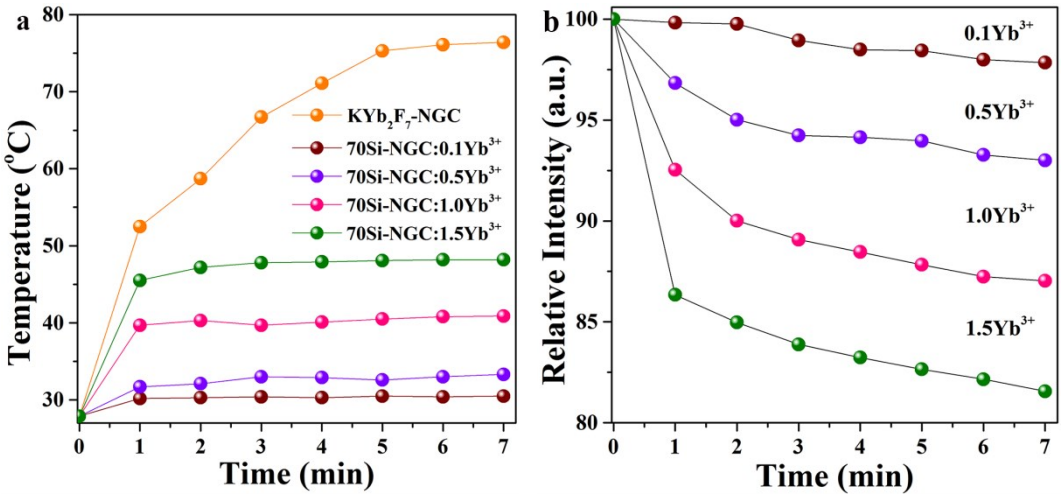


**Figure S7.** (a) Temperature curves of $Yb^{3+}$ doped 70Si-NGCs and $KYb_2F_7$ NGC irradiated by 980 nm laser diode for various times. The temperatures in the surface of $Yb^{3+}$ doped 70Si-NGCs increase when they were irradiated by 980 nm laser with power density of 44.6 W/cm$^2$ for 1 min. Then the temperatures of samples are stable due to the heat dissipation to the air. Obviously, the highest temperatures of the 70Si-GCs increase monotonously with the doping concentration of $Yb^{3+}$ due to the superfluous absorption of 980 nm lasers. For the $KYb_2F_7$ NGC, the temperature increase to 52 $^o$C when it was irradiated by 980 nm laser just for 1 min. Then the temperature sequentially increase to 75 $^o$C by the further irradiation of laser due to the high concentration (6.0 mol%) of $Yb^{3+}$ in the GC. (b) Relative intensity of the UC emission of $xYb^{3+}$ (x=0.1-1.5) doped 70Si-NGCs as a function of the irradiated times by 980 nm lasers. The emission intensity of $Yb^{3+}$-$Yb^{3+}$ pairs decrease due to the thermal quenching of luminescence and the attenuation rate of the emission intensity increases with the doping concentration of $Yb^{3+}$ ions. These results indicate that the thermal effect irradiated by the 980 nm laser is stronger in highly-doped sample and that is bad for the luminescence of $Yb^{3+}$-$Yb^{3+}$ pairs.

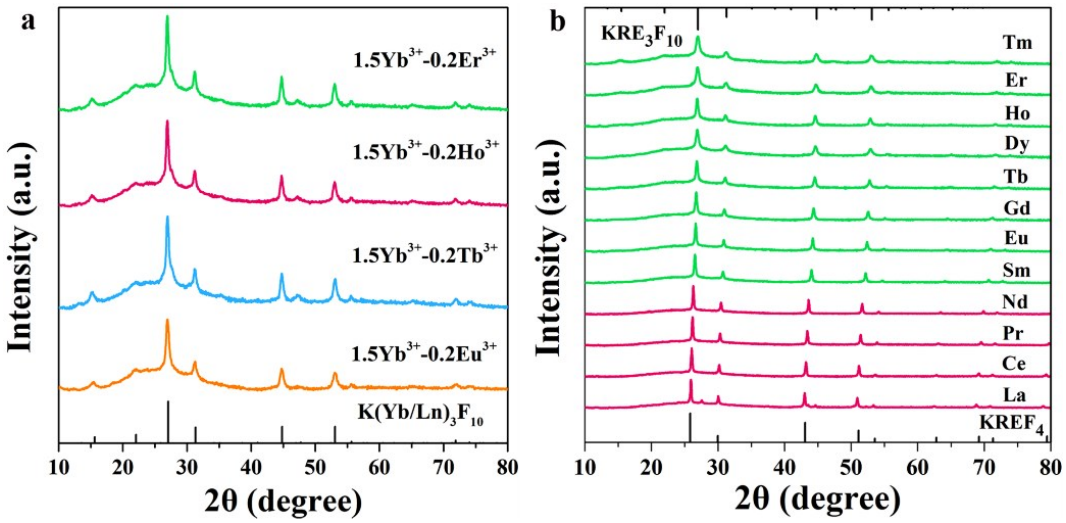


**Figure S8.** (a) XRD patterns of $1.5Yb^{3+}$-$0.2Ln^{3+}$ doped 70Si-NGCs. (Ln=Eu, Tb, Ho, Tm and Er) The XRD patterns of the co-doped NGCs match well with the JCPDS Cards of $K(Yb/Ln)F_{10}$ crystals, indicating $K(Yb/Ln)F_{10}$ nanocrystals have been precipitated in the NGCs via the heat treatments. (b) XRD patterns of 1.5 mol% RE ions doped 70Si-NGCs. (RE=Tm-La) Various RE-fluoride nanocrystals are precipitated in the RE ions doped 70Si-NGC depended on the dopant species. Cubic $KRE_3F_{10}$ nanocrystals are precipitated in the NGCs when the doped RE ions (from $Yb^{3+}$ to $Sm^{3+}$) possess small ionic radius. While for the RE ions (from $Nd^{3+}$ to $La^{3+}$) possessing lager ionic radius and smaller potential, cubic $KREF_4$ nanocrystals are controllably precipitated in the NGCs.

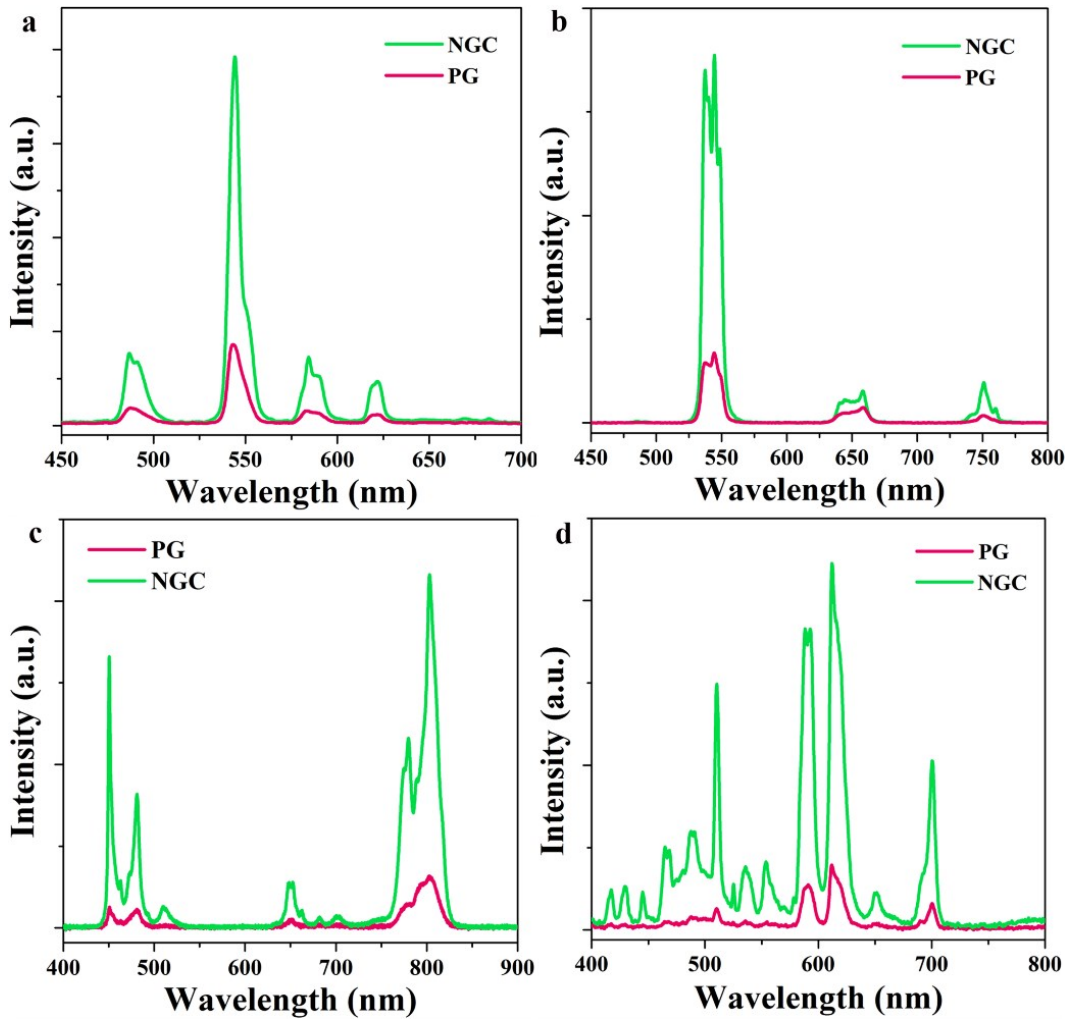


**Figure S9.** UC emission spectra of (a) $1.5Yb^{3+}$-$0.2Tb^{3+}$, (b) $1.5Yb^{3+}$-$0.2Ho^{3+}$, (c) $1.5Yb^{3+}$-$0.025Tm^{3+}$ and (d) $1.5Yb^{3+}$-$0.2Eu^{3+}$ co-doped PGs and NGCs. Excited by using a 980 nm laser diode, the UC emission intensity in the codoped NGCs are all dramatically enhanced, as compared to the corresponding PGs.

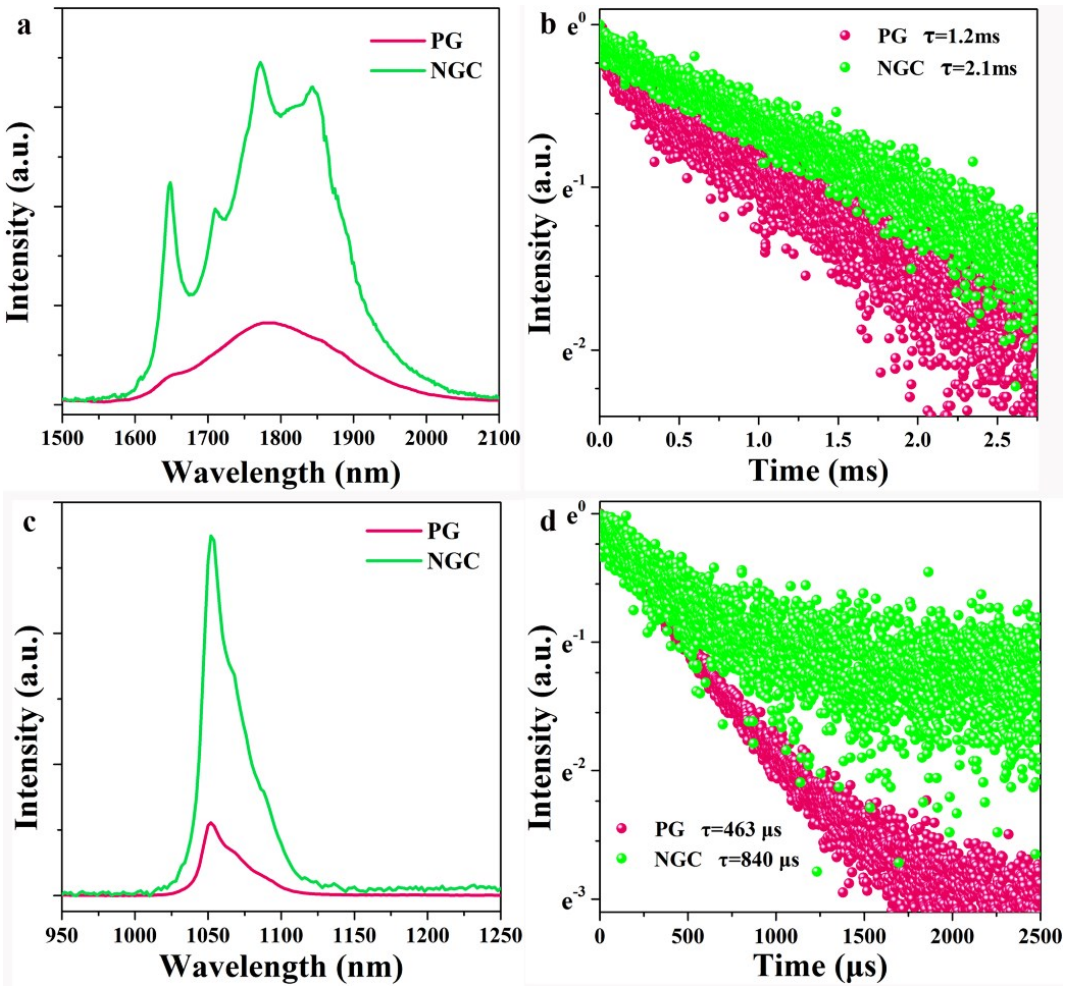


**Figure S10.** (a) Emission spectra excited by 808 nm lasers and (b) emission decay curves monitored at 1800 nm emissions of 0.1$Tm^{3+}$ doped 70Si-PG and NGC. (c) Emission spectra excited by 808 nm lasers and (d) emission decay curves monitored at 1060 nm emissions of 0.1$Nd^{3+}$ doped 70Si-PG and NGC. The down-shifting emission intensities and lifetimes in $Tm^{3+}$ and $Nd^{3+}$ doped NGCs are all enhanced in comparison with the corresponding PGs.

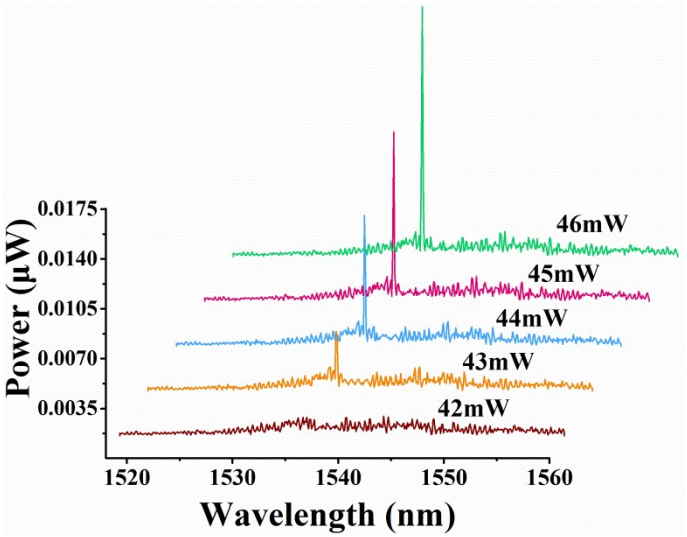


**Figure S11.** Lasing spectrum of PG microsphere pumped with various powers. The near-infrared fluorescence of $Er^{3+}$ from 1520 to 1560 nm is observed in the output spectra of PG when the pump power is low. Single-mode laser peaks around 1535 nm are observed when the pump power exceeds the threshold value (43 mW). The lasing output power increases from 0.0042 to 0.018 μW when the pump power is increased from 43 to 46 mW.

References

[1] Fang, Z.; Chormaic, S. N.; Wang, S.; Wang, X.; Yu, J.; Jiang, Y.; Qiu, J.; Wang, P. Bismuth-doped glass microsphere lasers. *Photonics Res*. **2017**, 5, 740.

[2] Vollmayr-Lee, K. Introduction to molecular dynamics simulations. *Am. J. Phys*. **2020**, 88, 401.